Refined Low-Energy Supernova Constraints on Lepton Flavor Violating Axions

Zi-Miao Huang, a Changqian Li, a Zuowei Liu a

^aDepartment of Physics, Nanjing University, Nanjing 210093, China E-mail: zimiaohuang@smail.nju.edu.cn, changqianli@smail.nju.edu.cn, zuoweiliu@nju.edu.cn

ABSTRACT: The supernova (SN) core, characterized by its extreme temperature and density, serves as a unique laboratory for new-physics searches. Low-energy supernovae (LESNe) provide particularly powerful probes, as their low explosion energies place stringent limits on any additional energy deposition in the mantle by new particles. We present refined LESN constraints on lepton-flavor-violating (LFV) axions and axion-like particles (ALPs) with electron-muon couplings. We consider four production channels in the SN: muon decay, lepton bremsstrahlung, electron-muon coalescence, and semi-Compton scattering, the last of which is investigated here for the first time in the context of LFV-ALPs. We find that muon decay dominates in the low-mass regime, electron-muon coalescence in the high-mass regime, and semi-Compton scattering in the intermediate-mass range. To derive accurate limits, we compute both the energy transfer from the SN core to the mantle and the energy loss due to ALP production in the mantle, which can be substantial for both large and small couplings—the latter case, to our knowledge, not previously noted in the literature. We find that LESNe provide the most stringent constraints on the parameter space for ALP masses above ~ 110 MeV. These refined results strengthen previous SN bounds and highlight the exceptional sensitivity of LESNe to LFV new physics.

Co	ontents	
1	Introduction	1
2	Model	3
3	Energy deposition in the mantle	3
	3.1 ALP production in the core	3
	3.2 ALP production in the mantle	5
4	SN profiles	5
5	ALP production	6
	5.1 Muon decay	7
	5.2 Lepton bremsstrahlung	7
	5.3 Electron-muon coalescence	8
	5.4 Semi-Compton scattering	9
	5.5 Comparison between different production channels	11
6	ALP absorption rate	12
7	LESN constraints	13
	7.1 Energy drain in the mantle	15
8	Summary	16
A	ALP momentum	16

1 Introduction

Axions are hypothetical pseudoscalar bosons that arise in extensions of the Standard Model, originally proposed to solve the strong CP problem [1–4]. Besides the original axions, a wide class of pseudoscalar particles—collectively referred to as axion-like particles (ALPs)—naturally emerge in numerous well-motivated new physics models beyond the Standard Model [5–8]. While most ALP searches focus on flavor-conserving couplings, lepton-flavor-violating (LFV) interactions can naturally arise from various ultraviolet completions or radiative corrections [6, 7, 9–16]. At the GeV scale and above, colliders and fixed-target facilities have placed stringent bounds on LFV-ALPs [17–25]. In the sub-GeV regime, muon decay experiments [26–38], and supernova (SN) observations [34, 39–41] provide leading constraints on ALPs that have an LFV coupling to electrons and muons.

In this work, we study constraints on LFV-ALPs from low-energy supernovae (LESNe), a class of underluminous Type II-P explosions with ejecta energies as low as 0.1 B =

10⁵⁰ erg, i.e., roughly 10-100 times dimmer than typical core-collapse SNe [42]. LESNe have been identified both observationally [43–53] and in simulations [54–62]. Unlike the conventional SN cooling bounds, which require that exotic energy losses not exceed the neutrino luminosity [63], LESN limits constrain the total energy deposited by new particles in the mantle to remain below the explosion energy of 0.1 B [42, 64, 65]. Recent analyses have shown that LESNe can provide powerful probes of new light particles [41, 42, 66–74].

Previous works have explored SN constraints on LFV-ALPs, including both the SN cooling limits [34, 39, 40] and the LESN limits [41]. However, Ref. [41] focused exclusively on LFV-ALPs with masses $m_a > m_\mu + m_e$, where only the electron-muon coalescence channel and its inverse process (ALP decay) were considered for production and absorption, respectively. In this paper, we extend the analysis to the full parameter space, including the regime $m_a < m_\mu + m_e$, where we incorporate four production processes: (1) muon decay, (2) lepton bremsstrahlung, (3) electron-muon coalescence, and (4) semi-Compton scattering. The semi-Compton scattering was recently found to contribute significantly to axions that couple to electrons [74].

It has been recently pointed out that for strong couplings, energy outflows from the mantle to both the core and the exterior of the progenitor can be substantial [73]. We include these effects to obtain more reliable LESN constraints in the large-coupling regime. For LFV-ALPs, we find that the energy drain from the mantle due to ALP production within it can be substantial not only in the strong coupling regime but also in the weak coupling regime—a feature that, to our knowledge, has not been recognized in previous studies. Moreover, a proper treatment of ALP absorption is crucial for deriving accurate LESN constraints. In Ref. [41], the survival probability along an ALP trajectory was approximated by evaluating the local absorption rate at the production point. Here, we explicitly integrate the absorption rate along the full ALP propagation path, leading to a more accurate evaluation of survival probability. Finally, while Ref. [41] used the Garching SN profiles [75, 76] at one second post-bounce, we employ the Garching SN profiles spanning the full 10-second post-bounce evolution, thus providing a more robust bound.

The rest of the paper is organized as follows. In Section 2 we introduce the LFV-ALP model. In Section 3 we compute the energy deposition in the SN mantle, including both the positive contributions from ALPs produced in the SN core and the negative contributions from ALPs produced in the mantle. Section 4 provides a brief introduction to the Garching group's muonic SN model SFHo-18.8. We compute the ALP production rate in Section 5, where we consider four different production channels: (1) muon decay, (2) lepton bremsstrahlung, (3) electron-muon coalescence, and (4) semi-Compton scattering. We then compute the ALP absorption rate in Section 6. We present our results in Section 7, and summarize our main findings in Section 8. Finally, Appendix A contains the detailed derivation of the Mandelstam variables for the semi-Compton scattering.

2 Model

We consider the LFV-ALP model which has the following interaction with electrons and muons: [41]

$$\mathcal{L}_{\text{int}} = \frac{g_{ae\mu}}{m_e^0 + m_\mu} \bar{e} \gamma^\lambda \gamma_5 \mu \partial_\lambda a + \text{h.c.}, \qquad (2.1)$$

where a denotes the ALP field, e and μ are the electron and muon fields, respectively, $m_e^0 = 0.511$ MeV is the electron mass in vacuum, $m_{\mu} = 105.6$ MeV is the muon mass, and $g_{ae\mu}$ is the dimensionless coupling constant. Note that the interaction Lagrangian in Eq. (2.1) is equivalent to the following interaction Lagrangian

$$\mathcal{L}_{\text{int}} = -ig_{ae\mu}a\bar{e}\gamma_5\mu + \text{h.c.}, \tag{2.2}$$

when the fermions are on-shell [40, 77-79]. We use the interaction Lagrangian in Eq. (2.2) in analysis.

3 Energy deposition in the mantle

ALPs can be copiously produced in the SN core owing to the extreme temperature and density conditions. As they propagate outward, a fraction of these ALPs are reabsorbed in the surrounding mantle, thereby transferring energy from the core to the mantle, which contributes to the SN explosion energy. On the other hand, ALPs produced in the mantle can transfer energy back to the core or outside the progenitor star, resulting in an energy drain from the mantle, which is particularly significant for strong couplings [73]. Thus, the net energy deposition in the SN mantle is given by [73]

$$E_d = E_c - E_m, (3.1)$$

where E_c denotes the energy transferred to the mantle by ALPs produced in the core, and E_m represents the energy loss from the mantle due to ALPs generated within it.

3.1 ALP production in the core

We first compute the energy transferred to the mantle by ALPs originating from the core. The net energy deposition in the mantle due to these core-produced ALPs is defined as the difference between the energy escaping the core surface and that escaping the progenitor's outer boundary [40, 42, 80]:

$$E_c = \int dt \int_0^{R_c} dr \int_{m'_a(r)}^{\infty} dE_a \frac{dL_a(r, E_a, t)}{dr dE_a} \left[\left\langle e^{-\tau_a(R_c, E_a, r)} \right\rangle - \left\langle e^{-\tau_a(R_*, E_a, r)} \right\rangle \right], \quad (3.2)$$

where t is time, r is the radial coordinate of ALP production, E_a is the ALP energy, τ_a is the optical depth, $L_a(r, E_a, t)$ is the ALP luminosity, $m'_a(r) = m_a/\text{lapse}(r)$ with m_a being the ALP mass and lapse(r) being the gravitational lapse function [42], and R_c and R_* are the radius of the core and the progenitor star, respectively. The two terms inside the brackets in Eq. (3.2) describe the ALP survival probability (due to reabsorption effects) at

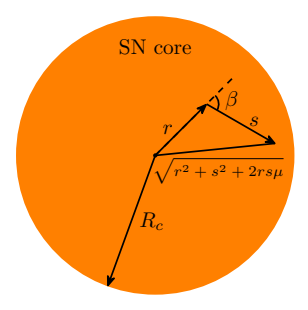


Figure 1. Schematic plot of the production position r, the propagation distance s, and the angle β inside the SN core.

 R_c and R_* , respectively. In our analysis we use $R_c = 20 \,\mathrm{km}$ and $R_* = 5 \times 10^8 \,\mathrm{km}$, which corresponds to the progenitor radius for the Garching group's muonic model SFHo-18.8 [42].

The ALP optical depth is given by (see e.g., Refs. [73, 80, 81])

$$\tau_a(R, E_a, r, \mu) = \int_0^{s_{\text{max}}} \frac{ds}{v} \Gamma\left(E_a, \sqrt{r^2 + s^2 + 2rs\mu}\right),\tag{3.3}$$

where v is the ALP velocity, s is the propagation distance, $\Gamma = \Gamma_A - \Gamma_E$ is the reduced ALP absorption rate with Γ_A (Γ_E) being the absorption (emission) rate, and $s_{\rm max} = \sqrt{R^2 - r^2(1 - \mu^2)} - r\mu$, where $\mu \equiv \cos \beta$ with β being the angle between the ALP trajectory and the outward radial direction; see Fig. 1 for a schematic plot of the production position r, the propagation distance s, and the angle β inside the SN core. Note that $\sqrt{r^2 + s^2 + 2rs\mu}$ denotes the radial coordinate along the trajectory. Assuming isotropic propagation, one obtains the averaged survival probability [40, 80, 81]

$$\left\langle e^{-\tau_a(R,E_a,r)} \right\rangle = \int_{-1}^1 \frac{d\mu}{2} e^{-\tau_a(R,E_a,r,\mu)}.$$
 (3.4)

The ALP luminosity per unit radial distance per unit energy is given by ¹

$$\frac{dL_a(r, E_a, t)}{dr dE_a} = 4\pi r^2 \operatorname{lapse}(r)^2 (1 + 2v_r) E_a \frac{d^2 n_a}{dt dE_a},$$
(3.5)

where $d^2n_a/dtdE_a$ is the ALP production rate per unit volume per unit energy, and v_r is the radial velocity of the medium. Because $v_r \ll 1$ [42], in our analysis we neglect v_r in Eq. (3.5). The emission rate is related to the production rate via

$$\Gamma_E = \frac{2\pi^2}{|\mathbf{p}_a|E_a} \frac{d^2 n_a}{dt dE_a},\tag{3.6}$$

where $|\mathbf{p}_a| = \sqrt{E_a^2 - m_a^2}$.

¹Note that the dimension of luminosity is the same as dE/dt, and $4\pi r^2 dr$ is the volume of the spherical shell between r and r + dr.

3.2 ALP production in the mantle

We next compute the energy drain by ALPs produced in the mantle. ALPs generated in the mantle and subsequently absorbed in the core or escaping the progenitor star lead to an energy loss from the mantle [73]:

$$E_m = E_m^{(1)} + E_m^{(2)}, (3.7)$$

where $E_m^{(1)}$ and $E_m^{(2)}$ denote the energy transferred from the mantle to the core and to the exterior of the progenitor, respectively. Following Ref. [73], we compute $E_m^{(1)}$ as follows:

$$E_m^{(1)} = \int dt \int_{R_c}^{R_*} dr \int_{m'_a(r)}^{\infty} dE_a \frac{dL_a(r, E_a, t)}{dr dE_a} \times \int_{1}^{-\sqrt{1 - R_c^2/r^2}} \frac{d\mu}{2} e^{-\tau'_a(E_a, r, \mu)} \left[1 - e^{-\tau''_a(E_a, r, \mu)} \right], \tag{3.8}$$

where

$$\tau_a'(E_a, r, \mu) = \int_0^{s_1} \frac{ds}{v} \Gamma\left(E_a, \sqrt{r^2 + s^2 + 2rs\mu}\right)$$
 (3.9)

is the optical depth between the ALP production point and the entry point into the core, and

$$\tau_a''(E_a, r, \mu) = \int_{s_1}^{s_2} \frac{ds}{v} \Gamma\left(E_a, \sqrt{r^2 + s^2 + 2rs\mu}\right)$$
 (3.10)

is the optical depth within the core. The two integration limits in Eqs. (3.9)and (3.10) are given by $s_{1,2} = -r\mu \mp [R_c^2 - r^2(1-\mu^2)]^{1/2}$, which correspond to the entry and exit points of the core. We compute $E_m^{(2)}$ as follows:

$$E_m^{(2)} = \int dt \int_{R_c}^{R_*} dr \int_{m_a'(r)}^{\infty} dE_a \frac{dL_a(r, E_a, t)}{dr \, dE_a} \left\langle e^{-\tau_a(R_*, E_a, r)} \right\rangle. \tag{3.11}$$

Note that for $m_a > m_\mu + m_e^0$ and sufficiently large couplings, ALPs decay mostly within the progenitor via $a \to e^{\mp} \mu^{\pm}$, resulting in the approximation $E_m^{(2)} \approx 0$.

4 SN profiles

Due to plasma effects, the electron mass in the SN core is modified so that it deviates significantly from its vacuum value, $m_e^0 = 0.511$ MeV. The in-medium electron mass is given by [78, 82]:

$$m_e = \frac{m_e^0}{\sqrt{2}} + \sqrt{\frac{(m_e^0)^2}{2} + \frac{\alpha}{\pi}(\mu_e^2 + \pi^2 T^2)},$$
 (4.1)

where $\alpha = 1/137$ is the fine structure constant.

To compute the ALP production and absorption rates, we adopt the radial distributions and temporal evolution of various physical quantities from the SFHo-18.8 model [75, 76]. The left panel of Fig. 2 displays the spatial evolution of temperature T, electron chemical potential μ_e , muon chemical potential μ_μ , proton chemical potential μ_p , proton interaction potential U_p , in-medium proton mass m_p^* , gravitational lapse factor, and the in-medium

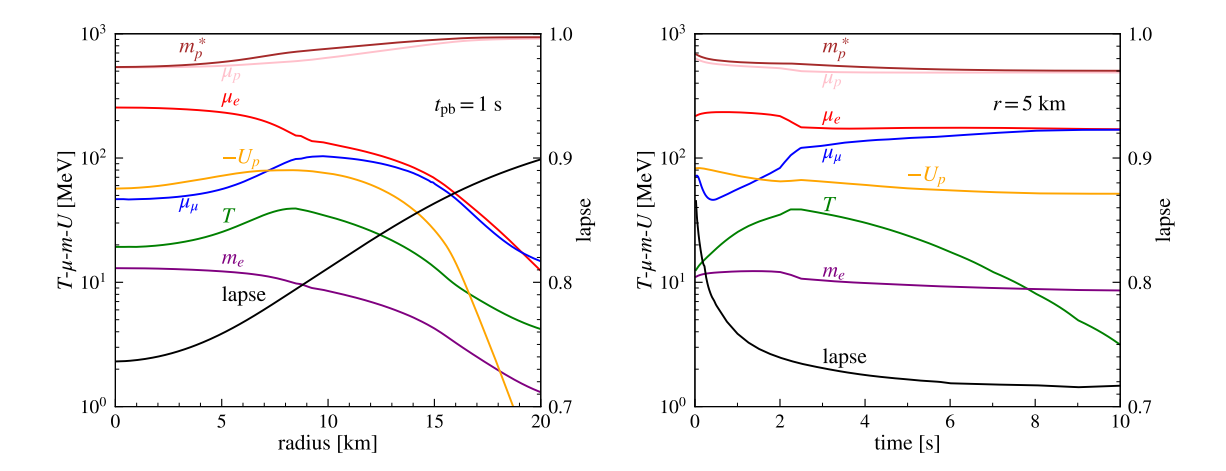


Figure 2. Left: Spatial evolution of the Garching profiles for the SFHo-18.8 SN model [76] at 1 s post-bounce. Right: Temporal evolution of the same model at a fixed radial distance of r = 5 km, spanning 10 seconds post-bounce. The displayed profiles include the temperature T, the electron chemical potential μ_e , the muon chemical potential μ_p , the negative of the proton interaction potential U_p , the in-medium proton mass m_p^* , the proton chemical potential μ_p which includes m_p^* [40], the gravitational lapse factor, and the in-medium electron mass m_e calculated using Eq. (4.1).

electron mass m_e calculated using Eq. (4.1) at $t_{\rm pb} = 1$ s with $t_{\rm pb}$ denoting the post-bounce time. The right panel of Fig. 2 shows the time evolution of the same quantities at a fixed radial distance of r = 5 km, spanning 10 seconds post-bounce.

5 ALP production

In this section we compute ALP production in the SN core and mantle for the following four processes: (1) muon decay $\mu \to e+a$, (2) lepton bremsstrahlung $\mu(e)+p\to e(\mu)+p+a$, (3) electron-muon coalescence $e+\mu\to a$, and (4) semi-Compton $\mu(e)+\gamma\to e(\mu)+a$. While these processes are possible for both leptons and antileptons, we focus on lepton-induced reactions due to their significantly higher abundance in the SN core. The sole exception is electron-muon coalescence, which inherently requires both a lepton and an antilepton in the initial state. Fig. 3 shows the Feynman diagrams for muon decay, lepton bremsstrahlung, and electron-muon coalescence; Fig. 4 shows the Feynman diagrams for semi-Compton. Note that muon decay is kinematically allowed only for ALP masses satisfying $m_a < m_\mu - m_e$; electron-muon coalescence requires $m_a > m_\mu + m_e$. Lepton bremsstrahlung and semi-Compton have no such mass constraints. Also note that there are two important lepton bremsstrahlung processes: $e^- + p \to \mu^- + p + a$ and $\mu^- + p \to e^- + p + a$; following Ref. [40], we consider the latter only for $m_\mu < m_a + m_e$.

²In the mass range of $m_{\mu} > m_a + m_e$, the fermion (either electron or muon) propagator in the $\mu^- + p \to e^- + p + a$ process can be on-shell, if the virtual photon momentum goes to zero. In such cases, $\mu^- + p \to e^- + p + a$ effectively becomes the muon decay process.

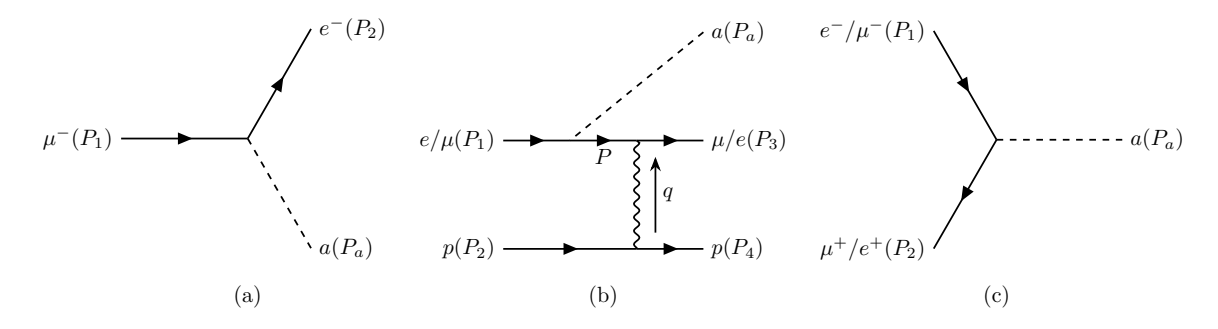


Figure 3. Production processes of LFV-ALP in the SN: (a) muon decay, (b) lepton bremsstrahlung, and (c) $e-\mu$ coalescence.

5.1 Muon decay

The Feynman diagram for the muon decay process $\mu^-(P_1) \to e^-(P_2) + a(P_a)$ is shown in Fig. 3 (a). The muon decay process can only occur if the mass condition $m_{\mu} > m_e + m_a$ is satisfied. The LFV-ALP production rate per unit volume per unit energy is given by [40]

$$\frac{d^2 n_d}{dt dE_a} = \frac{|\mathcal{M}_d|^2}{32\pi^3} \int_{E_2^-}^{E_2^+} dE_2 f_\mu^- (1 - f_e^-), \tag{5.1}$$

where $|\mathcal{M}_d|^2 = 2g_{ae\mu}^2[(m_\mu - m_e)^2 - m_a^2]$ is the spin-summed squared matrix element, $f_\ell^- = \left[e^{(E_\ell - \mu_\ell)/T} + 1\right]^{-1}$ is the Fermi-Dirac distribution for fermion ℓ^- , and the integration limits are

$$E_2^{\pm} = \frac{E_a(m_{\mu}^2 - m_e^2 - m_a^2)}{2m_a^2} \pm \frac{\sqrt{E_a^2 - m_a^2}}{2m_a^2} I(m_{\mu}, m_e, m_a), \tag{5.2}$$

where

$$I(x, y, z) = \sqrt{(x^2 - y^2 - z^2)^2 - 4y^2 z^2}.$$
 (5.3)

5.2 Lepton bremsstrahlung

We now consider the lepton bremsstrahlung processes:

$$e^{-}(P_1) + p(P_2) \to \mu^{-}(P_3) + p(P_4) + a(P_a),$$
 (5.4)

$$\mu^{-}(P_1) + p(P_2) \to e^{-}(P_3) + p(P_4) + a(P_a),$$
 (5.5)

as shown in Fig. 3 (b). The ALP production rate per unit volume per unit energy is given by [40, 78, 79]

$$\frac{d^2 n_b}{dt dE_a} = \frac{n_{\text{eff}} |\mathbf{p}_a|}{(2\pi)^6 32 m_p^2} \int_{m_3}^{\infty} dE_3 \int_{-1}^{1} dz_a dz_3 \int_{0}^{2\pi} d\phi |\mathbf{p}_1| |\mathbf{p}_3| f_1 (1 - f_3) |\mathcal{M}_b|^2, \tag{5.6}$$

where ϕ is the angle between the \mathbf{p}_1 - \mathbf{p}_a plane and the \mathbf{p}_1 - \mathbf{p}_3 plane, $z_a = \cos \theta_{1a}$ with θ_{1a} being the angle between \mathbf{p}_1 and \mathbf{p}_a , $z_3 = \cos \theta_{13}$ with θ_{13} being the angle between \mathbf{p}_1 and \mathbf{p}_3 , n_{eff} is the effective proton number density, and \mathcal{M}_b is the matrix element. Since the proton mass is much larger than the core temperature, $T \sim 30 \text{ MeV}$, proton recoil can be neglected.

Following Refs. [40, 83], we adopt the static-proton approximation $E_2 \simeq E_4 \simeq m_p$, which yields $|\mathbf{p}_1| = \sqrt{(E_3 + E_a)^2 - m_1^2}$. The effective proton number density is given by [78, 79]

$$n_{\text{eff}} = 2 \int \frac{d^3 p_2}{(2\pi)^3} f_p(E_2) [1 - f_p(E_2)],$$
 (5.7)

where

$$f_p(E_p) = \frac{1}{e^{(E_p - \mu_p)/T} + 1}$$
 (5.8)

is the proton distribution function, with E_p (μ_p) being the proton energy (chemical potential). Taking into account plasma effects, the proton energy E_p is given by

$$E_p = \sqrt{m_p^{*2} + \mathbf{p}_2^2} + U_p, \tag{5.9}$$

where m_p^* is the in-medium proton mass and U_p is the proton interaction potential. Note that we have used the approximation $\mathbf{p}_2 \simeq \mathbf{p}_4$ [40] in obtaining Eq. (5.7), and used Garching profiles [76] for m_p^* , μ_p , and U_p , which are shown in Fig. 2. The matrix element for the lepton bremsstrahlung processes takes the form as

$$i\mathcal{M}_b = 2e^2 g_{ae\mu} m_p \frac{1}{|\mathbf{q}|\sqrt{\mathbf{q}^2 + k_s^2}} \left[\bar{u}_3 \gamma^0 \frac{\not P + m_3}{P^2 - m_3^2} \gamma_5 u_1 + \bar{u}_3 \gamma_5 \frac{\not Q + m_1}{Q^2 - m_1^2} \gamma^0 u_1 \right], \tag{5.10}$$

where $P = P_1 - P_a$, $Q = P_3 + P_a$, and $k_s^2 = (4\pi\alpha/T)\sum_j Z_j^2 n_j$ is the Debye screening scale with n_j being the number density of ion j with charge $Z_j e$ [84].

5.3 Electron-muon coalescence

For ALPs with masses $m_a > m_\mu + m_e$, the electron-muon coalescence can occur, which consists of two processes: $e^-(P_1) + \mu^+(P_2) \to a(P_a)$ and $\mu^-(P_1) + e^+(P_2) \to a(P_a)$, as shown in Fig. 3 (c). In both processes, we denote the four-momenta of the initial-state particles as P_1 (fermion) and P_2 (anti-fermion). The ALP production rate per unit volume per unit energy is [40]

$$\frac{d^2 n_c}{dt dE_a} = \frac{|\mathcal{M}_c|^2}{32\pi^3} \int_{E_2^-}^{E_2^+} dE_2 \left(f_\mu^- f_e^+ + f_e^- f_\mu^+ \right), \tag{5.11}$$

with $|\mathcal{M}_c|^2 = 2g_{ae\mu}^2[m_a^2 - (m_\mu - m_e)^2]$, and $f_\ell^+ = \left[e^{(E_\ell + \mu_\ell)/T} + 1\right]^{-1}$ is the Fermi-Dirac distribution for anti-fermion ℓ^+ . The integration limits E_2^{\pm} for the anti-fermion energy are determined by:

$$E_2^{\pm} = \frac{E_a(m_a^2 - m_1^2 + m_2^2)}{2m_a^2} \pm \frac{\sqrt{E_a^2 - m_a^2}}{2m_a^2} I(m_1, m_2, m_a), \tag{5.12}$$

where m_1 and m_2 represent the fermion and anti-fermion masses, respectively, and I is given by Eq. (5.3).

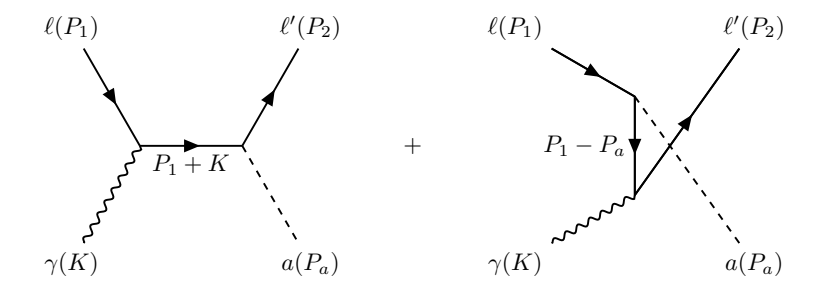


Figure 4. The Feynman diagrams for the semi-Compton scattering $\ell + \gamma \to \ell' + a$.

5.4 Semi-Compton scattering

Recently, Ref. [74] points out that semi-Compton scattering provide significant contributions to axions that couple to electrons. In this section, we calculate the LFV-ALP production from the semi-Compton scattering.

The matrix element for the semi-Compton scattering $\ell(P_1) + \gamma(K) \to \ell'(P_2) + a(P_a)$ shown in Fig. 4 is given by

$$i\mathcal{M}_s = eg_{ae\mu}\epsilon^{\mu}_{\lambda}(K)\bar{u}(P_2)\left(\gamma_5 \frac{\not P_1 + \not K + m_{\ell}}{s - m_{\ell}^2}\gamma_{\mu} + \gamma_{\mu} \frac{\not P_1 - \not P_a + m_{\ell'}}{u - m_{\ell'}^2}\gamma_5\right)u(p), \tag{5.13}$$

where $s \equiv (p_1 + K)^2$ and $u \equiv (P_1 - P_a)^2$. The matrix element squared, summed with the final state spins, averaged with the initial state spins and polarizations, is

$$\frac{1}{4} \sum_{\text{spins},\lambda} |\mathcal{M}_s|^2 = e^2 g_{ae\mu}^2 \left[\frac{\langle \Phi_{ss} \rangle}{(s - m_\ell^2)^2} + \frac{\langle \Phi_{us} \rangle + \langle \Phi_{su} \rangle}{(s - m_\ell^2)(u - m_{\ell'}^2)} + \frac{\langle \Phi_{uu} \rangle}{(u - m_{\ell'}^2)^2} \right], \tag{5.14}$$

where

$$\langle \Phi_{ss} \rangle = m_{\ell}^2 (2m_a^2 + 2m_{\ell}m_{\ell'} - 3m_{\ell'}^2) + s(m_{\ell'}^2 - 2m_{\ell}^2 + 2m_{\ell}m_{\ell'}) + um_{\ell}^2 - us, \tag{5.15}$$

$$\langle \Phi_{su} \rangle = \langle \Phi_{us} \rangle = (m_{\ell'}^2 - m_{\ell}^2)(s - u) - us - 2m_{\ell}^2 m_{\ell'}^2$$

+
$$(m_a^2 + m_\ell m_{\ell'}) \left[2(m_\ell^2 + m_{\ell'}^2) - m_\ell m_{\ell'} - t \right],$$
 (5.16)

$$\langle \Phi_{uu} \rangle = m_{\ell}^2 (u - 3m_{\ell'}^2) + 2m_{\ell} m_{\ell'} (m_{\ell'}^2 + u) + m_{\ell'}^2 (2m_a^2 + s - 2u) - us.$$
 (5.17)

Here we have followed Ref. [74] by neglecting the plasma mass correction to the initial photon and treated it as massless. We note that Ref. [40] also carried out such an analysis, and our results agree with Ref. [40]; however, the cross term in Eq. (5.14) differs from Eq. (20) of Ref. [74] by an overall minus sign. Such an error leads to an overestimation of the semi-Compton scattering in Ref. [74].

The LFV-ALP production rate per unit volume per unit energy is [74]

$$\frac{d^2 n_s}{dt dE_a} = \int_0^\infty \frac{\mathbf{p}_1^2}{E_1} d|\mathbf{p}_1| \int_{\omega_p}^\infty |\mathbf{k}| d|\mathbf{k}| \int_{-1}^1 d\mu \int_0^{2\pi} d\phi \Theta(1 - |\cos \xi|) \times \frac{f_\ell(E_1) f_\gamma(|\mathbf{k}|) \left[1 - f_{\ell'}(E_1 + |\mathbf{k}| - E_a)\right]}{512\pi^6 |\mathbf{p}_1 + \mathbf{k}|} \sum_{\text{spins}, \lambda} |\mathcal{M}_s|^2, \tag{5.18}$$

where $f_{\gamma}(|\mathbf{k}|) = [\exp(|\mathbf{k}|/T) - 1]^{-1}$ is the Bose-Einstein distribution for photons, $\mu = \cos \theta$ with θ being the angle between \mathbf{p}_1 and \mathbf{k} , and $\xi(\phi)$ is the ALP polar (azimuthal) angle with respect to $\mathbf{p}_1 + \mathbf{k}$. The delta function associated with energy conservation leads to

$$\cos \xi = \frac{\mathbf{p}_1 \cdot \mathbf{k} + E_a E_1 + (E_a - E_1)|\mathbf{k}| + (m_{\ell'}^2 - m_{\ell}^2 - m_a^2)/2}{|\mathbf{p}_1 + \mathbf{k}||\mathbf{p}_a|}.$$
 (5.19)

For the lower integration limit of $|\mathbf{k}|$ in Eq. (5.18), we use the plasma frequency ω_p in the relativistic limit, which is given by [85]

$$\omega_p^2 = \frac{4\alpha}{3\pi} \left(\mu_e^2 + \frac{1}{3}\pi^2 T^2 \right). \tag{5.20}$$

We note that ω_p effectively removes the divergence in the $|\mathbf{k}| \to 0$ regime.

By solving $|\cos \xi| \le 1$, we derive the constraints on μ from Eq. (5.19) as

$$\mu_{\min} \equiv \frac{X_1 - X_2}{|\mathbf{p}_1||\mathbf{k}|} \le \mu \le \frac{X_1 + X_2}{|\mathbf{p}_1||\mathbf{k}|} \equiv \mu_{\max},$$
(5.21)

where

$$X_1 \equiv (E_a - E_1)(E_a - |\mathbf{k}|) + (m_\ell^2 - m_{\ell'}^2 - m_a^2)/2, \tag{5.22}$$

$$X_2 \equiv |\mathbf{p}_a| \sqrt{(E_1 + |\mathbf{k}| - E_a)^2 - m_{\ell'}^2}.$$
 (5.23)

Note that the square root in X_2 is always valid since $E_1 \geq E_a + m_{\ell'} - |\mathbf{k}|$ is guaranteed by the energy conservation. Thus, the LFV-ALP production rate per unit volume per unit energy is given by

$$\frac{d^2 n_s}{dt dE_a} = \int_0^\infty \frac{\mathbf{p}_1^2}{E_1} d|\mathbf{p}_1| \int_{k_{\min}}^\infty |\mathbf{k}| d|\mathbf{k}| \int_{\mu_{\min}}^{\mu_{\max}} d\mu \Theta(1 - |\mu|) \int_0^{2\pi} d\phi \times \frac{f_\ell(E_1) f_\gamma(|\mathbf{k}|) \left[1 - f_{\ell'}(E_1 + |\mathbf{k}| - E_a)\right]}{512\pi^6 |\mathbf{p}_1 + \mathbf{k}|} \sum_{\text{spins}, \lambda} |\mathcal{M}_s|^2,$$
(5.24)

where $k_{\min} = \max\{E_a + m_{\ell'} - E_1, \omega_p\}$. Although Eqs. (5.18) and (5.24) are identical analytically, we prefer to use Eq. (5.24) for numerical calculations since the Heaviside function here only constrains a single integration variable μ explicitly, unlike the Heaviside function in Eq. (5.18), which constrains the three integration variables $|\mathbf{p}_1|$, $|\mathbf{k}|$, and μ implicitly.

To compute the production rate, we express the Mandelstam variables s and t in terms of the integration variables:

$$s = (P_1 + K)^2 = m_\ell^2 + 2|\mathbf{k}|(E_1 - |\mathbf{p}_1|\mu), \tag{5.25}$$

$$t = (K - P_a)^2 = m_a^2 + 2|\mathbf{k}| [|\mathbf{p}_a|(\cos \xi \cos \zeta - \sin \xi \cos \phi \sin \zeta) - E_a], \qquad (5.26)$$

where $\cos \zeta = (|\mathbf{p}_1|\mu + |\mathbf{k}|)/|\mathbf{p}_1 + \mathbf{k}|$, and $\sin \zeta = |\mathbf{p}_1|\sqrt{1-\mu^2}/|\mathbf{p}_1 + \mathbf{k}|$. The derivation of these expressions is provided in appendix A. We then determine the Mandelstam variable u via

$$u = m_{\ell}^2 + m_{\ell'}^2 + m_a^2 - s - t. (5.27)$$

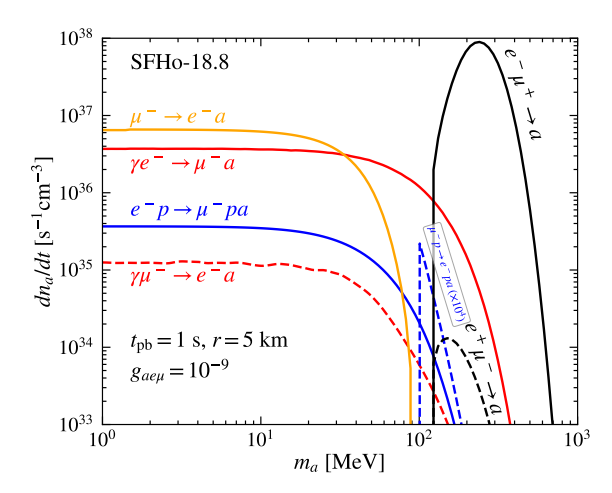


Figure 5. LFV-ALP production rates per unit volume at $t_{\rm pb}=1$ s and r=5 km with $g_{ae\mu}=10^{-9}$ from various channels: (1) muon decay $\mu^- \to e^- a$ (solid orange), (2) lepton bremsstrahlung $e^- p \to \mu^- pa$ (solid blue) and $\mu^- p \to e^- pa$ (dashed blue), (3) electron-muon coalescence $e^- \mu^+ \to a$ (solid black) and $e^+ \mu^- \to a$ (dashed black), and (4) semi-Compton scattering $\gamma e^- \to \mu^- a$ (solid red) and $\gamma \mu^- \to e^- a$ (dashed red). We use the Garching group's muonic model SFHo-18.8. The $\mu^- p \to e^- pa$ channel is shown for masses above ~ 100 MeV (multiplied with a factor of 10^4) since we require $m_e + m_a > m_\mu$ for this channel to avoid double counting with muon decay.

5.5 Comparison between different production channels

To compare different production channels, we compute the LFV-ALP production rate per unit volume via

$$\frac{dn_a}{dt} = \int_{m_a}^{\infty} dE_a \frac{dn_a}{dt dE_a},\tag{5.28}$$

where $dn_a/dtdE_a$ is the production rate per unit volume per unit energy. Fig. 5 shows the LFV-ALP production rates per unit volume from different production channels at one second post-bounce and r=5 km with $g_{ae\mu}=10^{-9}$. The muon decay process $\mu^- \to e^- a$ dominates for $m_a \lesssim 30$ MeV, the electron-muon coalescence process $e^- \mu^+ \to a$ dominates for $m_a \gtrsim 110$ MeV, and the semi-Compton scattering process $e^- \gamma \to \mu^- a$ dominates in the intermediate mass range 30 MeV $\lesssim m_a \lesssim 110$ MeV. The lepton bremsstrahlung process is always subdominant. For the lepton bremsstrahlung, electron-muon coalescence, and semi-Compton scattering processes, the production rates involving an initial electron are greater than those involving an initial muon, due to the higher electron number density.

We also plot the production rate per unit volume from the semi-Compton scattering processes varying with the radial coordinate r at $t_{\rm pb}=1$ s, as shown in the left panel of Fig. 6, where we fix $m_a=1$ MeV and $g_{ae\mu}=10^{-9}$. We find that the LFV-ALP production rate per unit volume from $\gamma e^- \to \mu^- a$ dominates over that from $\gamma \mu^- \to e^- a$ for $r \lesssim 7$ km, where the electron and muon chemical potentials are comparable. Conversely, for $r \gtrsim 7$ km, the production rate from $\gamma \mu^- \to e^- a$ becomes dominant.

We further compute the total LFV-ALP production rates within the SN core via

$$4\pi \int_0^{R_c} dr r^2 \frac{dn_a}{dt},\tag{5.29}$$

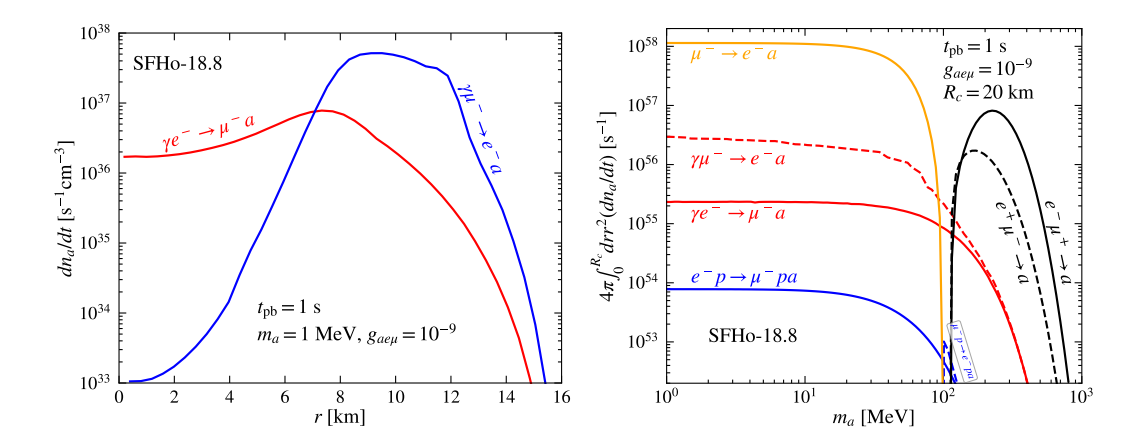


Figure 6. Left panel: The LFV-ALP production rate per unit volume from the semi-Compton scattering processes $\gamma e^- \to \mu^- a$ (red) and $\gamma \mu^- \to e^- a$ (blue) varying with the radial coordinate at $t_{\rm pb}=1$ s for $m_a=1$ MeV and $g_{ae\mu}=10^{-9}$. Right panel: The total LFV-ALP production rates within the SN core, $4\pi \int_0^{R_c} dr r^2 (dn_a/dt)$, at $t_{\rm pb}=1$ s with $g_{ae\mu}=10^{-9}$ from various channels: (1) muon decay $\mu^- \to e^- a$ (solid orange), (2) lepton bremsstrahlung $e^- p \to \mu^- pa$ (solid blue) and $\mu^- p \to e^- pa$ (dashed blue), (3) electron-muon coalescence $e^- \mu^+ \to a$ (solid black) and $e^+ \mu^- \to a$ (dashed black), and (4) semi-Compton scattering $\gamma e^- \to \mu^- a$ (solid red) and $\gamma \mu^- \to e^- a$ (dashed red). We use the Garching group's muonic model SFHo-18.8.

where dn_a/dt is given in Eq. (5.28). The right panel of Fig. 6 shows the total LFV-ALP production rates within the SN core at $t_{\rm pb}=1$ s with $g_{ae\mu}=10^{-9}$ from various channels. The muon decay process $\mu^- \to e^- a$ dominates for $m_a \lesssim 90$ MeV, the electron–muon coalescence process $e^-\mu^+ \to a$ dominates for $m_a \gtrsim 110$ MeV, and the semi-Compton scattering process $\gamma\mu^- \to e^- a$ dominates in the intermediate mass range 90 MeV $\lesssim m_a \lesssim 110$ MeV. The lepton bremsstrahlung process remains subdominant throughout the entire mass range. For electron–muon coalescence, the production rate involving an initial electron exceeds that with an initial muon, while for lepton bremsstrahlung and semi-Compton scattering, the rates involving an initial electron are likewise higher than those involving an initial muon.

6 ALP absorption rate

In this section we compute the ALP absorption rate. Figs. 7 and 8 show the ALP absorption processes: (1) electron-ALP coalescence, (2) inverse bremsstrahlung, (3) ALP decay, and (4) inverse semi-Compton. These ALP absorption processes are the inverse processes of the ALP production processes, as shown in Figs. 3 and 4.

The ALP absorption rate can be obtained from the production rate of the inverse process as [40]

$$\Gamma_A(E_a) = e^{(E_a - \mu_a^0)/T} \Gamma_E = e^{(E_a - \mu_a^0)/T} \frac{2\pi^2}{|\mathbf{p}_a| E_a} \frac{d^2 n_a}{dt dE_a},\tag{6.1}$$

where $E_a = \sum_i E_i - \sum_{j \neq a} E_j$ and $\mu_a^0 \equiv \sum_i \mu_i - \sum_{j \neq a} \mu_j$ with i (j) denoting the final (initial) particles in the absorption process. We note that the reduced absorption rate can

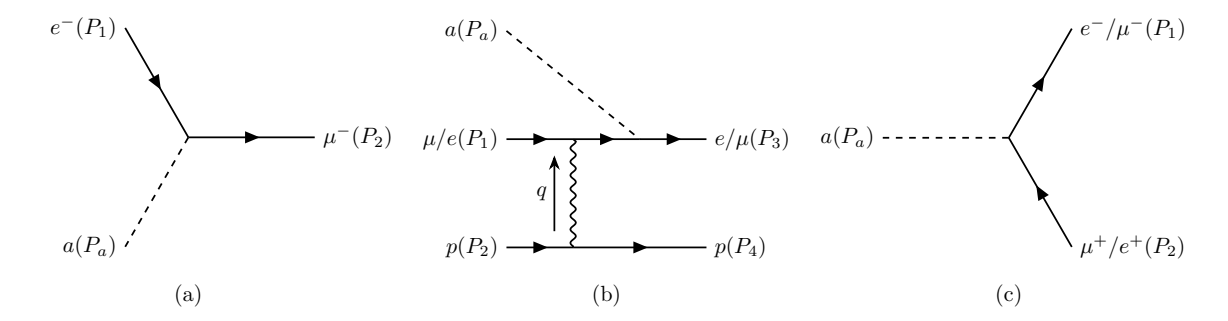


Figure 7. Absorption processes of LFV-ALP in the SN: (a) electron-ALP coalescence, (b) inverse bremsstrahlung, and (c) ALP decay, which are the inverse processes of the three production processes shown in Fig. 3.

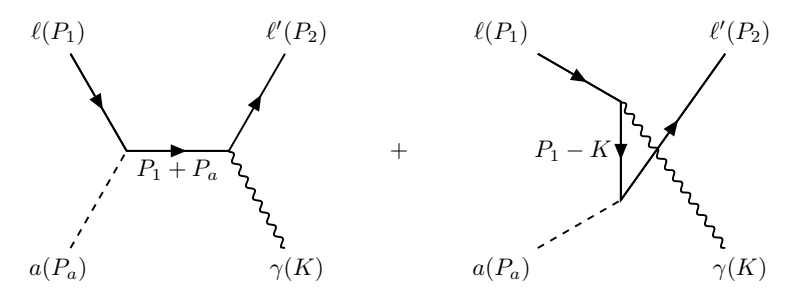


Figure 8. The Feynman diagrams for the inverse semi-Compton scattering $a + \ell \rightarrow \ell' + \gamma$, which are the inverse processes of the semi-Compton scattering shown in Fig. 4.

be determined solely by the absorption rate via $\Gamma = \Gamma_A - \Gamma_E = \left[1 - e^{-(E_a - \mu_a^0)/T}\right] \Gamma_A$.

In the large mass region $m_a > m_{\mu} + m_e$, the dominant absorption process is $a \to e^{\mp} \mu^{\pm}$ (ALP decay). In this case, for the absorption term up to the progenitor radius (the second term in brackets in Eq. (3.2)), we approximate the ALP decay rate with its vacuum value:

$$\Gamma_A^{\text{vac}} = \frac{g_{ae\mu}^2 [m_a^2 - (m_\mu - m_e^0)^2]}{4\pi m_a^2 E_a} I(m_a, m_\mu, m_e^0).$$
 (6.2)

This is because both temperature and mass density decline steeply beyond the core such that ALPs effectively decay in vacuum.

7 LESN constraints

We compute the LESN constraints on LFV-ALPs by demanding that the net energy deposition E_d in the SN mantle, calculated via Eq. (3.1), does not exceed the LESN explosion energy: $E_d \leq 0.1$ B. We consider four ALP production processes: (1) muon decay, (2) lepton bremsstrahlung, (3) electron-muon coalescence, and (4) semi-Compton scattering.

Fig. 9 shows the LESN constraints on LFV-ALPs, derived under the condition $E_d \leq$ 0.1 B. We also show existing bounds, including those from rare muon decay experiments [26, 27, 29, 30, 33] and SN cooling [40].

In the low-mass region ($m_a \lesssim 100$ MeV), the most stringent constraints arise from rare muon decay experiments [26, 27, 29, 30, 33], which probe the coupling $g_{ae\mu}$ down to the

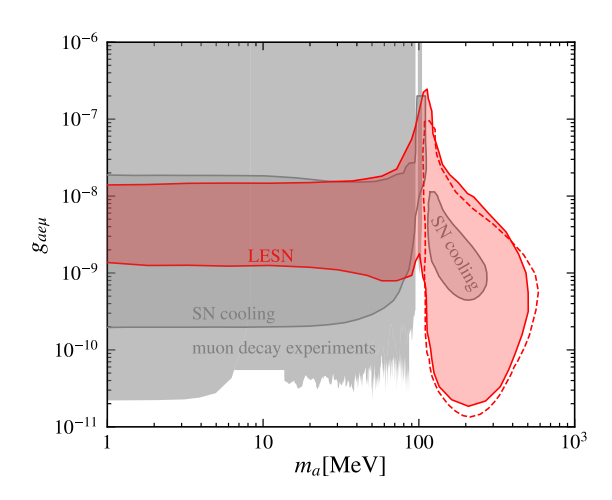


Figure 9. The LESN constraints on LFV-ALPs for $E_d \leq 0.1$ B (red-shaded). Also shown are the LESN constraints derived in Ref. [41] (red-dashed). Gray-shaded regions are constraints derived from SN cooling bounds [40] and rare muon decay experiments [26, 27, 29, 30, 33], which are taken from Ref. [40].

level of $\sim 10^{-11}$. The next most stringent constraints come from SN cooling limits [40], while the LESN bounds reach only $g_{ae\mu} \sim 10^{-9}$, about one order of magnitude weaker. This outcome runs contrary to the naive expectation based on the energy budget, since the LESN explosion energy (~ 0.1 B) is approximately three orders of magnitude smaller than the upper bound on the ALP energy escaping from the SN core in the cooling analyses (~ 100 B), suggesting that the LESN energy budget should, in principle, lead to a tighter constraint. The weaker LESN limits instead reflect the inefficient absorption of ALPs in the mantle. In the low-mass region, the relevant absorption processes (namely electron–ALP coalescence, inverse bremsstrahlung, and inverse semi-Compton scattering) depend on the electron or muon number densities, both of which decrease rapidly with radius outside the SN core. Consequently, most ALPs produced in the core escape the progenitor star without being reabsorbed, leading to weaker LESN limits despite the tighter energy budget.

For ALPs with masses above the kinematic threshold of $m_a > m_\mu + m_e$, the muon decay channel is kinematically forbidden, and the corresponding rare muon decay limits are therefore inapplicable. In this mass range, SN observations provide the most stringent constraints, and the dominant ALP production channel in the SN is the electron-muon coalescence process. We find that LESNe probe a broader region of parameter space than the SN cooling limits, which is opposite to the trend observed in the low-mass regime. This difference arises mainly because, in the high-mass region, the dominant ALP absorption channel is ALP decay, whose rate increases with the radial coordinate r in the SN mantle, leading to highly efficient absorption in this region. Our current analysis shows that LESNe can probe the $g_{ae\mu}$ coupling down to $\sim 2 \times 10^{-11}$ at $m_a \simeq 200$ MeV, which is about a factor of two weaker than the previous LESN result in Ref. [41], shown as the red-dashed contour in Fig. 9. This difference arises mainly because the present analysis employs the Garching SN profiles spanning the full ten-seconds post-bounce evolution, whereas Ref. [41] used

only the one-second post-bounce profile. In addition, the current analysis adopts a more accurate treatment of ALP absorption, by performing explicit trajectory integrations.

For ALPs with masses in the range $m_{\mu} - m_{e} < m_{a} < m_{\mu} + m_{e}$, both muon decay and electron-muon coalescence are kinematically forbidden. In this intermediate mass region, the dominant production channel is the semi-Compton scattering process, as shown in Fig. 5. Since the in-medium electron mass is ~13 MeV at r=20 km and decreases to ~1 MeV at r=50 km, this mass window corresponds approximately to $m_{a} \simeq (100,110)$ MeV. Within this range, we find that the LESNe provide the most stringent constraints, excluding the $g_{ae\mu}$ coupling down to ~ 10^{-9} .

7.1 Energy drain in the mantle

In Fig. 10, we compare the LESN constraints obtained with and without accounting for the energy drain in the mantle, the E_m term in Eq. (3.1). We find that neglecting this contribution leads to a much larger excluded parameter space. We find that for strong couplings, the inclusion of the E_m term has a pronounced impact and can modify the constraints on $g_{ae\mu}$ by more than an order of magnitude. Interestingly, for ALP masses below ~ 100 MeV, the effects of the E_m term remain substantial even in the weak-coupling regime, a feature that, to our knowledge, has not been emphasized in previous studies. This behavior arises because, for $m_a \lesssim m_\mu + m_e$, the ALP decay process is kinematically forbidden, allowing the LFV-ALPs produced in the mantle to escape the progenitor star nearly freely, thereby causing a significant energy loss. Overall, these findings highlight the importance of properly including the mantle energy-drain effect in deriving reliable LESN constraints on LFV-ALPs for both strong and weak couplings.

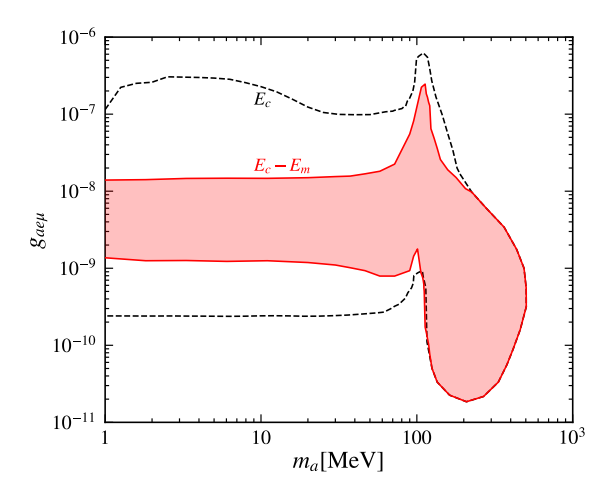


Figure 10. Comparison of LESN constraints with (red-solid) and without (black-dashed) accounting for the energy drain in the mantle.

We note that in the regime of large couplings, LFV-ALPs can reach equilibrium with the medium. In this case, the requirement of a vanishing ALP chemical potential implies $\mu_e = \mu_\mu$. In our present analysis, however, we use the Garching group's muonic model SFHo-18.8, where the electron and muon chemical potentials are not equal. A more accurate

determination of the limits in the strong-coupling regime would therefore require a more sophisticated treatment that self-consistently accounts for these effects, which we leave for future work.

8 Summary

In this paper, we present refined LESN constraints on LFV-ALPs. We consider four production channels in the SN: muon decay, lepton bremsstrahlung, electron-muon coalescence, and semi-Compton scattering, the last of which is analyzed here for the first time for LFV-ALPs in the SN. We find that muon decay and electron-muon coalescence dominate the ALP production in the small and large mass regimes, respectively, and semi-Compton scattering provides leading contributions in the intermediate mass range. The lepton bremsstrahlung process is found to be subdominant. We compute the net energy deposition in the SN mantle by taking into account both the energy transfer from the core to the mantle and the energy drain from the mantle due to ALP production within it. We find that the energy drain from the mantle are substantical for both strong- and weak-coupling regimes, the latter of which, to our knowledge, has not been noted in the literature. By requiring the net energy deposited in the SN mantle to be less than the LESN explosion energy (0.1 B), and by properly accounting for ALP absorption using the Garching group's muonic model SFHo-18.8, which spans about ten seconds post-bounce, we obtain more accurate LESN constraints. We find that LESNe can provide the most stringent constraints on LFV-ALPs with masses above ~ 110 MeV.

Acknowledgments

We thank Yonglin Li, Wenxi Lu, and Zicheng Ye for discussions. We thank Hans-Thomas Janka for providing the SN profiles used for numerical calculations. The work is supported in part by the National Natural Science Foundation of China under Grant No. 12275128.

A ALP momentum

In this section we express the Mandelstam variables in the semi-Compton scattering in terms of the integration variables. We work in the frame F where the z-axis is along the momentum of the initial photon \mathbf{k} and the momentum of the initial charged lepton \mathbf{p}_1 is in the xz-plane. In the frame F we have

$$K^{\mu} = |\mathbf{k}|(1, 0, 0, 1), \quad P_1^{\mu} = (E_1, |\mathbf{p}_1| \sin \theta, 0, |\mathbf{p}_1| \cos \theta).$$
 (A.1)

where θ is the polar angle of \mathbf{p}_1 . To obtain the ALP momentum, we work in another frame F' where the z'-axis is along $\mathbf{p}_1 + \mathbf{k}$ and the y'-axis is the same as the y-axis in the F frame, as shown in Fig. 11. In the frame F', we have

$$P_a^{\prime\mu} = (E_a, |\mathbf{p}_a| \sin \xi \cos \phi, |\mathbf{p}_a| \sin \xi \sin \phi, |\mathbf{p}_a| \cos \xi), \tag{A.2}$$

where $\xi(\phi)$ is the ALP polar (azimuthal) angle in the F' frame.

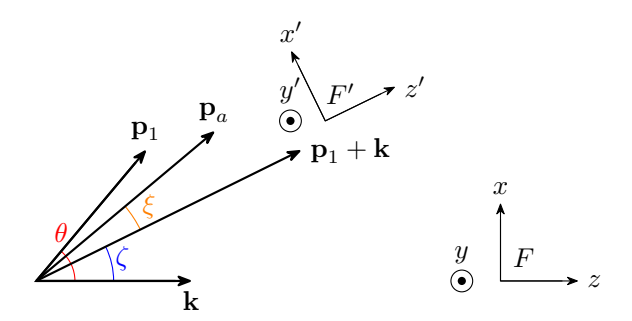


Figure 11. The momentum directions of the initial charged lepton (\mathbf{p}_1) and photon (\mathbf{k}) , and the final ALP (\mathbf{p}_a) .

The transformation from the frame F to F' is a clockwise rotation around the y-axis by an angle ζ , which is determined by

$$\cos \zeta = \frac{(\mathbf{p}_1 + \mathbf{k}) \cdot \mathbf{k}}{|\mathbf{p}_1 + \mathbf{k}||\mathbf{k}|} = \frac{|\mathbf{p}_1| \cos \theta + |\mathbf{k}|}{|\mathbf{p}_1 + \mathbf{k}|}, \quad \sin \zeta = \frac{|\mathbf{p}_1| \sin \theta}{|\mathbf{p}_1 + \mathbf{k}|}. \tag{A.3}$$

In this case, $|\mathbf{p}_a|_y = |\mathbf{p}'_a|_{y'}$, and

$$|\mathbf{p}_{a}|_{x} = |\mathbf{p}'_{a}|_{x'}\cos\zeta + |\mathbf{p}'_{a}|_{z'}\sin\zeta = |\mathbf{p}_{a}|(\sin\xi\cos\phi\cos\zeta + \cos\xi\sin\zeta), \tag{A.4}$$

$$|\mathbf{p}_a|_z = |\mathbf{p}_a'|_{z'}\cos\zeta - |\mathbf{p}_a'|_{x'}\sin\zeta = |\mathbf{p}_a|(\cos\xi\cos\zeta - \sin\xi\cos\phi\sin\zeta). \tag{A.5}$$

The three Mandelstam variables are then given by

$$s = (P_1 + K)^2 = m_\ell^2 + 2|\mathbf{k}|(E_1 - |\mathbf{p}_1|\cos\theta), \tag{A.6}$$

$$t = (K - P_a)^2 = m_a^2 + 2|\mathbf{k}| \left[|\mathbf{p}_a|(\cos\xi\cos\zeta - \sin\xi\cos\phi\sin\zeta) - E_a \right], \tag{A.7}$$

$$u = m_{\ell}^2 + m_{\ell'}^2 + m_a^2 - s - t. \tag{A.8}$$

References

- [1] R. D. Peccei and H. R. Quinn, "CP Conservation in the Presence of Instantons," Phys. Rev. Lett. 38 (1977) 1440–1443.
- [2] F. Wilczek, "Problem of Strong P and T Invariance in the Presence of Instantons," Phys. Rev. Lett. **40** (1978) 279–282.
- [3] S. Weinberg, "A New Light Boson?" Phys. Rev. Lett. 40 (1978) 223–226.
- [4] M. Kuster, G. Raffelt, and B. Beltran, eds., "The Strong CP problem and axions," Lect. Notes Phys. **741** (2008) 3–17 [hep-ph/0607268].
- [5] G. B. Gelmini and M. Roncadelli, "Left-Handed Neutrino Mass Scale and Spontaneously Broken Lepton Number," Phys. Lett. B 99 (1981) 411–415.
- [6] A. Davidson and K. C. Wali, "MINIMAL FLAVOR UNIFICATION VIA MULTIGENERATIONAL PECCEI-QUINN SYMMETRY," Phys. Rev. Lett. 48 (1982) 11.
- [7] F. Wilczek, "Axions and Family Symmetry Breaking," Phys. Rev. Lett. 49 (1982) 1549–1552.
- [8] P. Svrcek and E. Witten, "Axions In String Theory," JHEP 06 (2006) 051 [hep-th/0605206].

- [9] A. A. Anselm, N. G. Uraltsev, and M. Y. Khlopov, "mu —> e FAMILON DECAY," Sov. J. Nucl. Phys. 41 (1985) 1060.
- [10] J. L. Feng, T. Moroi, H. Murayama, and E. Schnapka, "Third generation familions, b factories, and neutrino cosmology," Phys. Rev. D 57 (1998) 5875–5892 [hep-ph/9709411].
- [11] M. Bauer, T. Schell, and T. Plehn, "Hunting the Flavon," Phys. Rev. D 94 (2016) 056003 [arXiv:1603.06950].
- [12] Y. Ema, K. Hamaguchi, T. Moroi, and K. Nakayama, "Flaxion: a minimal extension to solve puzzles in the standard model," JHEP **01** (2017) 096 [arXiv:1612.05492].
- [13] L. Calibbi, F. Goertz, D. Redigolo, R. Ziegler, and J. Zupan, "Minimal axion model from flavor," Phys. Rev. D **95** (2017) 095009 [arXiv:1612.08040].
- [14] K. Choi, S. H. Im, C. B. Park, and S. Yun, "Minimal Flavor Violation with Axion-like Particles," JHEP 11 (2017) 070 [arXiv:1708.00021].
- [15] M. Chala, G. Guedes, M. Ramos, and J. Santiago, "Running in the ALPs," Eur. Phys. J. C 81 (2021) 181 [arXiv:2012.09017].
- [16] M. Bauer, M. Neubert, S. Renner, M. Schnubel, and A. Thamm, "The Low-Energy Effective Theory of Axions and ALPs," JHEP 04 (2021) 063 [arXiv:2012.12272].
- [17] M. Endo, S. Iguro, and T. Kitahara, "Probing $e\mu$ flavor-violating ALP at Belle II," JHEP **06** (2020) 040 [arXiv:2002.05948].
- [18] S. Iguro, Y. Omura, and M. Takeuchi, "Probing $\mu\tau$ flavor-violating solutions for the muon q-2 anomaly at Belle II," JHEP **09** (2020) 144 [arXiv:2002.12728].
- [19] H. Davoudiasl, R. Marcarelli, N. Miesch, and E. T. Neil, "Searching for flavor-violating ALPs in Higgs boson decays," Phys. Rev. D **104** (2021) 055022 [arXiv:2105.05866].
- [20] K. Cheung, A. Soffer, Z. S. Wang, and Y.-H. Wu, "Probing charged lepton flavor violation with axion-like particles at Belle II," JHEP 11 (2021) 218 [arXiv:2108.11094].
- [21] H. Davoudiasl, R. Marcarelli, and E. T. Neil, "Lepton-flavor-violating ALPs at the Electron-Ion Collider: a golden opportunity," JHEP **02** (2023) 071 [arXiv:2112.04513].
- [22] T. Araki, K. Asai, H. Otono, T. Shimomura, and Y. Takubo, "Search for lepton flavor violating decay at FASER," JHEP 01 (2023) 145 [arXiv:2210.12730].
- [23] L. Calibbi, Z. Huang, S. Qin, Y. Yang, and X. Yin, "Testing axion couplings to leptons in Z decays at future e+e- colliders," Phys. Rev. D 108 (2023) 015002 [arXiv:2212.02818].
- [24] B. Batell, H. Davoudiasl, R. Marcarelli, E. T. Neil, and S. Trojanowski, "Lepton-Flavor-Violating ALP Signals with TeV-Scale Muon Beams." arXiv:2407.15942.
- [25] L. Calibbi, T. Li, L. Mukherjee, and Y. Yang, "Probing ALP Lepton Flavour Violation at μ TRISTAN." arXiv:2406.13234.
- [26] S. E. Derenzo, "Measurement of the low-energy end of the mu-plus decay spectrum," Phys. Rev. 181 (1969) 1854–1866.
- [27] A. Jodidio et al., "Search for Right-Handed Currents in Muon Decay," Phys. Rev. D 34 (1986) 1967. [Erratum: Phys.Rev.D 37, 237 (1988)].
- [28] D. A. Bryman and E. T. H. Clifford, "EXOTIC MUON DECAY mu —> e x," Phys. Rev. Lett. **57** (1986) 2787.

- [29] R. Bilger et al., "Search for exotic muon decays," Phys. Lett. B 446 (1999) 363–367 [hep-ph/9811333].
- [30] TWIST Collaboration, "Search for two body muon decay signals," Phys. Rev. D 91 (2015) 052020 [arXiv:1409.0638].
- [31] M. Bauer, M. Neubert, S. Renner, M. Schnubel, and A. Thamm, "Axionlike Particles, Lepton-Flavor Violation, and a New Explanation of a_{μ} and a_{e} ," Phys. Rev. Lett. **124** (2020) 211803 [arXiv:1908.00008].
- [32] C. Cornella, P. Paradisi, and O. Sumensari, "Hunting for ALPs with Lepton Flavor Violation," JHEP **01** (2020) 158 [arXiv:1911.06279].
- [33] **PIENU** Collaboration, "Improved search for two body muon decay $\mu^+ \rightarrow e^+ X_H$," Phys. Rev. D **101** (2020) 052014 [arXiv:2002.09170].
- [34] L. Calibbi, D. Redigolo, R. Ziegler, and J. Zupan, "Looking forward to lepton-flavor-violating ALPs," JHEP **09** (2021) 173 [arXiv:2006.04795].
- [35] M. Bauer, M. Neubert, S. Renner, M. Schnubel, and A. Thamm, "Flavor probes of axion-like particles," JHEP **09** (2022) 056 [arXiv:2110.10698].
- [36] S. Knapen, T. Opferkuch, D. Redigolo, and M. Tammaro, "Displaced searches for Axion-Like Particles and Heavy Neutral Leptons at Mu3e," JHEP 06 (2025) 189 [arXiv:2410.13941].
- [37] Y. Jho, S. Knapen, and D. Redigolo, "Lepton-flavor violating axions at MEG II," JHEP 10 (2022) 029 [arXiv:2203.11222].
- [38] S. Knapen, K. Langhoff, T. Opferkuch, and D. Redigolo, "A robust search for lepton flavour violating axions at Mu3e," JHEP **07** (2025) 243 [arXiv:2311.17915].
- [39] H.-Y. Zhang, R. Hagimoto, and A. J. Long, "Neutron star cooling with lepton-flavor-violating axions," Phys. Rev. D 109 (2024) 103005 [arXiv:2309.03889].
- [40] Y. Li and Z. Liu, "Supernova constraints on lepton flavor violating ALPs." arXiv:2501.12075.
- [41] Z.-M. Huang and Z. Liu, "Low-energy supernova constraints on lepton flavor violating axions," JHEP 10 (2025) 024 [arXiv:2506.16922].
- [42] A. Caputo, H.-T. Janka, G. Raffelt, and E. Vitagliano, "Low-Energy Supernovae Severely Constrain Radiative Particle Decays," Phys. Rev. Lett. **128** (2022) 221103 [arXiv:2201.09890].
- [43] N. N. Chugai and V. P. Utrobin, "The nature of sn 1997d: low mass progenitor and weak explosion," Astron. Astrophys. **354** (2000) 557 [astro-ph/9906190].
- [44] A. Pastorello *et al.*, "Low luminosity type II supernovae: spectroscopic and photometric evolution," Mon. Not. Roy. Astron. Soc. **347** (2004) 74 [astro-ph/0309264].
- [45] A. Pastorello et al., "SN 2005cs in M51 II. Complete Evolution in the Optical and the Near-Infrared," Mon. Not. Roy. Astron. Soc. 394 (2009) 2266 [arXiv:0901.2075].
- [46] S. Spiro, et al., "Low luminosity Type II supernovae II. Pointing towards moderate mass precursors," Monthly Notices of the Royal Astronomical Society 439 (2014) 2873–2892.
- [47] O. Pejcha and J. L. Prieto, "On The Intrinsic Diversity of Type II-Plateau Supernovae," Astrophys. J. 806 (2015) 225 [arXiv:1501.06573].

- [48] H. Yang and R. A. Chevalier, "Evolution of the Crab nebula in a low energy supernova," Astrophys. J. 806 (2015) 153 [arXiv:1505.03211].
- [49] M. L. Pumo, et al., "Radiation-hydrodynamical modelling of underluminous type II plateau Supernovae," Mon. Not. Roy. Astron. Soc. 464 (2017) 3013–3020 [arXiv:1610.02981].
- [50] J. W. Murphy, Q. Mabanta, and J. C. Dolence, "A Comparison of Explosion Energies for Simulated and Observed Core-Collapse Supernovae," Mon. Not. Roy. Astron. Soc. 489 (2019) 641–652 [arXiv:1904.09444].
- [51] A. Burrows and D. Vartanyan, "Core-Collapse Supernova Explosion Theory," Nature **589** (2021) 29–39 [arXiv:2009.14157].
- [52] S. Yang et al., "A low-energy explosion yields the underluminous Type IIP SN 2020cxd," Astron. Astrophys. 655 (2021) A90 [arXiv:2107.13439].
- [53] R. S. Teja, et al., "SN 2021wvw: A Core-collapse Supernova at the Subluminous, Slower, and Shorter End of Type IIPs," Astrophys. J. 974 (2024) 44 [arXiv:2407.13207].
- [54] F. S. Kitaura, H.-T. Janka, and W. Hillebrandt, "Explosions of O-Ne-Mg cores, the Crab supernova, and subluminous type II-P supernovae," Astron. Astrophys. 450 (2006) 345–350 [astro-ph/0512065].
- [55] T. Fischer, S. C. Whitehouse, A. Mezzacappa, F. K. Thielemann, and M. Liebendorfer, "Protoneutron star evolution and the neutrino driven wind in general relativistic neutrino radiation hydrodynamics simulations," Astron. Astrophys. 517 (2010) A80 [arXiv:0908.1871].
- [56] T. Melson, H.-T. Janka, and A. Marek, "Neutrino-driven supernova of a low-mass iron-core progenitor boosted by three-dimensional turbulent convection," Astrophys. J. Lett. 801 (2015) L24 [arXiv:1501.01961].
- [57] D. Radice, A. Burrows, D. Vartanyan, M. A. Skinner, and J. C. Dolence, "Electron-Capture and Low-Mass Iron-Core-Collapse Supernovae: New Neutrino-Radiation-Hydrodynamics Simulations," Astrophys. J. 850 (2017) 43 [arXiv:1702.03927].
- [58] S. M. Lisakov, L. Dessart, D. J. Hillier, R. Waldman, and E. Livne, "Progenitors of low-luminosity Type II-Plateau supernovae," Mon. Not. Roy. Astron. Soc. 473 (2018) 3863–3881 [arXiv:1709.08673].
- [59] B. Müller, et al., "Three-Dimensional Simulations of Neutrino-Driven Core-Collapse Supernovae from Low-Mass Single and Binary Star Progenitors," Mon. Not. Roy. Astron. Soc. 484 (2019) 3307–3324 [arXiv:1811.05483].
- [60] A. Burrows, D. Radice, and D. Vartanyan, "Three-dimensional supernova explosion simulations of 9-, 10-, 11-, 12-, and 13-M⊙ stars," Mon. Not. Roy. Astron. Soc. 485 (2019) 3153-3168 [arXiv:1902.00547].
- [61] G. Stockinger et al., "Three-dimensional Models of Core-collapse Supernovae From Low-mass Progenitors With Implications for Crab," Mon. Not. Roy. Astron. Soc. 496 (2020) 2039–2084 [arXiv:2005.02420].
- [62] S. Zha, E. P. O'Connor, S. M. Couch, S.-C. Leung, and K. Nomoto, "Hydrodynamic simulations of electron-capture supernovae: progenitor and dimension dependence," Mon. Not. Roy. Astron. Soc. 513 (2022) 1317–1328 [arXiv:2112.15257].
- [63] G. G. Raffelt, Stars as laboratories for fundamental physics: The astrophysics of neutrinos, axions, and other weakly interacting particles. 1996.

- [64] S. W. Falk and D. N. Schramm, "Limits From Supernovae on Neutrino Radiative Lifetimes," Phys. Lett. B 79 (1978) 511.
- [65] A. Sung, H. Tu, and M.-R. Wu, "New constraint from supernova explosions on light particles beyond the Standard Model," Phys. Rev. D 99 (2019) 121305 [arXiv:1903.07923].
- [66] A. Lella, E. Ravensburg, P. Carenza, and M. C. D. Marsh, "Supernova limits on QCD axionlike particles," Phys. Rev. D 110 (2024) 043019 [arXiv:2405.00153].
- [67] J. Alda, G. Levati, P. Paradisi, S. Rigolin, and N. Selimovic, "Collider and astrophysical signatures of light scalars with enhanced τ couplings," JHEP **06** (2025) 008 [arXiv:2407.18296].
- [68] G. Chauhan, S. Horiuchi, P. Huber, and I. M. Shoemaker, "Low-energy supernovae bounds on sterile neutrinos," JCAP **03** (2025) 052 [arXiv:2309.05860].
- [69] G. Chauhan, S. Horiuchi, P. Huber, and I. M. Shoemaker, "Probing the sterile neutrino dipole portal with SN1987A and low-energy supernovae," Phys. Rev. D 110 (2024) 015007 [arXiv:2402.01624].
- [70] P. Carenza, G. Lucente, L. Mastrototaro, A. Mirizzi, and P. D. Serpico, "Comprehensive constraints on heavy sterile neutrinos from core-collapse supernovae," Phys. Rev. D 109 (2024) 063010 [arXiv:2311.00033].
- [71] D. F. G. Fiorillo and E. Vitagliano, "Self-Interacting Dark Sectors in Supernovae Can Behave as a Relativistic Fluid," Phys. Rev. Lett. 133 (2024) 251004 [arXiv:2404.07714].
- [72] C. Li, Z. Liu, W. Lu, and Z. Ye, "Low-energy supernova constraints on millicharged particles," JHEP **07** (2025) 116 [arXiv:2408.04953].
- [73] D. F. G. Fiorillo, T. Pitik, and E. Vitagliano, "Energy Transfer by Feebly Interacting Particles in Supernovae: The Trapping Regime," Phys. Rev. Lett. **135** (2025) 071005 [arXiv:2503.13653].
- [74] D. F. G. Fiorillo, T. Pitik, and E. Vitagliano, "Supernova production of axionlike particles coupling to electrons, reloaded," Phys. Rev. D 112 (2025) 083008 [arXiv:2503.15630].
- [75] R. Bollig, W. DeRocco, P. W. Graham, and H.-T. Janka, "Muons in Supernovae: Implications for the Axion-Muon Coupling," Phys. Rev. Lett. 125 (2020) 051104 [arXiv:2005.07141]. [Erratum: Phys.Rev.Lett. 126, 189901 (2021)].
- [76] "Garching core-collapse supernova research archive." https://wwwmpa.mpa-garching.mpg.de/ccsnarchive/.
- [77] G. Raffelt and D. Seckel, "Bounds on Exotic Particle Interactions from SN 1987a," Phys. Rev. Lett. 60 (1988) 1793.
- [78] G. Lucente and P. Carenza, "Supernova bound on axionlike particles coupled with electrons," Phys. Rev. D **104** (2021) 103007 [arXiv:2107.12393].
- [79] R. Z. Ferreira, M. C. D. Marsh, and E. Müller, "Strong supernovae bounds on ALPs from quantum loops," JCAP 11 (2022) 057 [arXiv:2205.07896].
- [80] A. Caputo, G. Raffelt, and E. Vitagliano, "Radiative transfer in stars by feebly interacting bosons," JCAP **08** (2022) 045 [arXiv:2204.11862].
- [81] A. Caputo, G. Raffelt, and E. Vitagliano, "Muonic boson limits: Supernova redux," Phys. Rev. D 105 (2022) 035022 [arXiv:2109.03244].

- [82] E. Braaten, "Neutrino emissivity of an ultrarelativistic plasma from positron and plasmino annihilation," apj **392** (1991) 70.
- [83] P. Carenza and G. Lucente, "Revisiting axion-electron bremsstrahlung emission rates in astrophysical environments," Phys. Rev. D 103 (2021) 123024 [arXiv:2104.09524].
- [84] G. G. Raffelt, "ASTROPHYSICAL AXION BOUNDS DIMINISHED BY SCREENING EFFECTS," Phys. Rev. D **33** (1986) 897.
- [85] E. Braaten and D. Segel, "Neutrino energy loss from the plasma process at all temperatures and densities," Phys. Rev. D 48 (1993) 1478–1491 [hep-ph/9302213].